Lab on a Chip

PAPER

View Article Online
View Journal | View Issue

Cite this: *Lab Chip*, 2025, **25**, 4396

Gut-on-chip methodology based on 3D-printed molds: a cost-effective and accessible approach†

Elise Delannoy, Aurélie Burette, Sébastien Janel, Sabine Poiret, Nathalie Deboosere, Catherine Daniel and Alexandre Grassart *

Gut-on-chips (GoC) represent a disruptive and promising technology to unravel the underlying mechanisms of gut health and pathology in physiologically relevant contexts. Researchers aiming to adopt this approach typically face a choice between purchasing expensive commercial microfluidic chips or building custom devices from scratch in their laboratories. However, designing such microfluidic systems requires specialized technical skills. Moreover, fabricating the master molds used in chip production is both costly and time-consuming, often requiring access to cleanroom facilities and advanced microfabrication equipment. Consequently, widespread adoption of GoC technology in biology and health research laboratories remains limited due to these technological and economic barriers. To address these challenges, we present the 3DP-μGut, an open-access, low-cost gut-on-chip platform fabricated using a standard desktop stereolithography (SLA) 3D printer. The device design is simple and user-friendly, making it accessible to a broad range of laboratories. The method has been optimized to allow the batch production of multiple chips with reproducible quality, suitable for biological experimentation. Furthermore, the device was improved to support high-resolution confocal live imaging and is compatible with various microfluidic pump systems, from basic to fully integrated setups. As a proof of concept, Caco-2 cells were cultured in the 3DP-μGut, and after 7 days of maturation, the cells formed a self-organized 3D epithelium mimicking *in vivo* structures. Finally, to showcase the system's versatility, *Lactiplantibacillus plantarum* and *Shigella flexneri* were introduced to demonstrate coculture and infection assays, respectively. This work highlights 3D printing as a powerful enabler of affordable, customizable GoC platforms.

Received 13th February 2025,
Accepted 27th June 2025

DOI: 10.1039/d5lc00147a

rsc.li/loc

1 Introduction

Organ-on-chips (OoC) are rapidly emerging as new standard *in vitro* models. Their ability to mimic human organs in terms of structure, functionality and mechanical or chemical stimulation makes them a powerful and versatile research tool. Their implementation requires interdisciplinary skills combining engineering, materials science and biology approaches to reproduce living and functional tissues. OoC technology is particularly relevant for studying intestinal function and pathology due to the complex mechanical and 3D cellular structuration of the gut. In recent years, gut-on-chip (GoC) models outperformed conventional *in vitro* culture systems in mimicking the gut *3D* microstructure and its specific dynamic microenvironment.[1] Nonetheless, widespread adoption of these models in biological laboratories has been delayed by the technological challenges associated with their fabrication.

The historical and conventional method for constructing OoC devices, including GoC models, consists in the soft lithography of polydimethylsiloxane (PDMS) on SU-8 and silicon-based molds. PDMS is a widely used and well validated material for tissue engineering and OoC,[2] it can be easily implemented in any lab for rapid microfluidic chip production. On the other hand, the fabrication of dry etched silicon or SU-8 mold requires heavy equipment and extensive specialized training. This process is very precise, achieving a nanometer resolution, but is yet very expensive and time consuming due to protocols with numerous steps.[3] Another critical limitation is its lack of geometrical liberty for the structures of such molds: they are restricted in height and only allow planar patterns with a rectangular cross section. Several new approaches have been proposed to simplify mold production and make it more accessible for biologist researchers. Subtractive methods, like micro milling of plastics and aluminum for instance,[4–6] or laser cutting[7,8] are more affordable and show good potential for microfluidic

Univ. Lille, CNRS, Inserm, CHU Lille, Institut Pasteur de Lille, U1019 – UMR 9017 – CIIL – Center for Infection and Immunity of Lille, F-59000 Lille, France.
E-mail: alexandre.grassart@inserm.fr

† Electronic supplementary information (ESI) available. See DOI: https://doi.org/10.1039/d5lc00147a

applications but are limited by their relatively low resolution (0.1 mm) and subsequent surface roughness.

In the past decade, SLA 3D printers have gathered a strong interest from the microfluidic and organ- on chip community because of their inexpensiveness and high resolution.[9–11] They rely on an additive manufacturing method, the photopolymerization of a photocurable ink in successive layers, allowing the creation of intricate microstructures. If 3D printed molds are already used for many microfluidic applications,[12,13] they still face some challenges for OoC approaches. Several groups have proposed 3D printed mold to build OoC devices.[14–17] However, several critical limitations have restricted its broader implementation in biological research settings. Chief among these is the surface roughness inherent to most 3D printing technologies, particularly stereolithography (SLA), which can affect the fidelity of microscale features, reduce optical clarity, and impair cell adhesion. In addition, the presence of uncured monomers or residual photoinitiators in printed resins can inhibit PDMS curing, resulting in incomplete crosslinking or adhesion between PDMS and the mold.[18] Notably, previous studies have also reported resin toxicity, where unpolymerized compounds leach into PDMS during molding and subsequently compromise cell viability within the microfluidic device.[19] Dimensional accuracy also poses a challenge, as variations in printing resolution and thermal deformation during post-processing can lead to inconsistencies across devices. Finally, demolding PDMS structures from complex 3D printed molds often results in damage or loss of fine features, especially when molds are not properly treated or reused multiple times.

We propose here a successful method, the 3DP-μGut, to build a GoC device at medium throughput based on 3D printed molds with general user equipment: a commercial 3D printer and resin. The chip layout was inspired from the largely adopted and successful design of Ingber and colleagues[20] divided in two connected parts with a top and bottom chamber. The channel was modified in a curved conduit to better accommodate the gut spatial geometry. The molds are designed for a good reproducibility and are reusable multiple times without alteration of the printed patterns. Each pair of molds (for the top and the bottom parts) allows the fabrication of nine GoC per batch. Our approach includes a post-printing treatment protocol consisting of solvent washing, thermal and UV curing, and silanization to mitigate both curing inhibition and resin leaching, thereby preserving biocompatibility. Mold designs were optimized for dimensional fidelity and feature reproducibility, with surface roughness levels compatible with high-resolution imaging. Moreover, the mechanical stability of the molds was preserved across more than 30 PDMS casting cycles. The final devices are optimized for imaging purposes thanks to a thin PDMS layer on the bottom side. Additionally, the microfluidic chip has been simplified and optimized to be compatible with plug and play solutions, implementable with minimal training, and is also suitable for more open instruments in the case of specific applications. 3DP-μGut devices were seeded with Caco-2 cells, a widely used intestine epithelial model, to assess their biocompatibility and their capacity to mimic the gut 3D architecture as observed in state-of-the-art models.[21] Lastly, to show the versatility and functional relevance of the developed 3DP-μGut platform, we evaluated the capacity of our model for two critical applications in microbiology: (i) culturing a human commensal probiotic widely used in the food industry, *Lactiplantibacillus plantarum* and (ii) infection of *Shigella flexneri*, a WHO-classified high-priority bacterial pathogen known to be human restricted and for which small animal are inefficiently infected to eventually directly demonstrating the functional and human physiological relevance of 3DP-μGut. Overall, we present a fabrication process that is simple, robust, affordable in producing gut-on-chip devices, and demonstrate its applicability in investigating key aspects of gut physiopathology.

2 Material and methods

2.1 COMSOL simulation

Shear stress inside the 3DP-μGut was evaluated using COMSOL (COMSOL Multiphysics 5.5, COMSOL Inc.). The simulated curved channel was 11 mm long, 750 μm wide and 750 μm high with a spatial period of 3 mm. The steady state was calculated with laminar flow physics. Navier stokes equations for incompressible flow were applied. The fluid flow was set at 60 μL h^{-1} and a non-slip condition was applied to the channel walls.

2.2 Mold printing, post-treatment, characterization

3DP-μGut molds were designed using Fusion 360 (Autodesk). For printing, STL files were uploaded in Preform software (Formlabs, USA), layer thickness was set to 25 μm, 50 μm, 100 μm and prints were directly performed on a build platform 2 using a Form 3 SLA 3D printer or a Form 4 MSLA 3D printer (Formlabs, USA). The molds were aligned parallel to the platform to achieve the smoothest possible surface. After careful removing from the build platform 2 and prints were washed to remove excess uncured resin with IPA for 20 min using FormWash (Formlabs, USA) and dried with air, followed by a UV post treatment using FormCure (Formlabs, USA). According to the resin used some molds also underwent thermal post treatment as detailed in the following table (Table 1).

The printed mold was then salinized by nebulization of trichloro(1*H*,1*H*,2*H*,2*H*-perfluorooctyl)silane (Sigma Aldrich, USA) under a vacuum during 2 hours, and heated at 90 °C for 1 h. The molds were imaged and measured with VHX-X1 microscope (Keyence, Japan). The height of the printed pattern was measured by focusing successively on the bottom and the top of the pattern. The 3D reconstruction of the ROI and measures of the height profile was calculated using the 3D module (Keyence, Japan).

Table 1 Post treatment recipes according to printer model and resin type

		UV post curing				Thermal baking	
Printer	Resin	Duration	Wavelength	Dose	Temperature	Duration	Temperature
FORM 3	Rigid 4000	15 min	405 nm	5.5 mW cm^{-2}	80 °C	—	—
	Clear V4	1 h	405 nm	5.5 mW cm^{-2}	60 °C	—	—
FORM 4	Clear V5	1 h	405 nm	5.5 mW cm^{-2}	60 °C	2 h	120 °C
	Black V5	15 min	405 nm	5.5 mW cm^{-2}	60 °C	2 h	120 °C
	Precision V1	5 min	405 nm	5.5 mW cm^{-2}	35 °C	2 h	120 °C

2.3 Chips fabrication and assembly

For chip fabrication, a ratio of 1 : 10 w/w of the curing agent and PDMS pre-polymer (Sylgard 184, Dow Corning, USA) was used. For the bottom molds, plexiglass sheet and a 500 g weight were placed on top to control the height of the resulting PDMS slab. PDMS was cured overnight at 65 °C. The PDMS was then carefully peeled of the molds surface, cut in individual parts.

The top compartments were exposed to O_2 plasma at 100 W, 50 kHz (Cute, Femto Science, South Korea) and bonded with a polyester (PET) porous membrane in the middle (ipCELLCULTURE™ track-etched membranes, pore size: 8 μm, it4ip, Belgium) previously treated by O_2 plasma 100 W, 50 kHz and 5% APTES (Sigma Aldrich, USA) at 75 °C for 20 min. The bottom compartments were then exposed to O_2 plasma 100 W, 50 kHz and aligned with the tops to complete the gut chip. The chips were washed successively with 70% ethanol and Milli Q water and then air dried. Eventually, chips were exposed to UVO (UVO cleaner, Jelight Company inc., USA) during 20 min for sterilization and stored in Petri dish before use.

2.4 Atomic force microscopy

Experiments were performed on a Bruker BioScope Resolve AFM coupled to a Zeiss Observer. Z1 optical microscope running NanoScope 9.4 software. PDMS surfaces were scanned in air either in contact mode using Bruker SNL-C probes or in soft tapping mode using RFESP probes at 0.6 Hz. 3D images were rendered using NanoScope data analysis software with no filter and with the same z-scale. Roughness was analyzed using the corresponding data analysis software for 100 × 100 μm scans. Arithmetic average roughness (R_a) gives a general indication of the surface's topography while root mean square roughness (R_q) informs about larger deviations (peaks and valleys) and captures surface texture variations more accurately.

$$R_a = \frac{1}{N}\sum_{i=1}^{N}|Z_i| \quad R_q = \sqrt{\left((1/N)\sum_{i=1}^{N}(Z_i)^2\right)}$$

where N is the number of pixels of the image and Z_i the height deviation from the mean surface plane.

2.5 Fluidic profile characterization

To characterize fluid flow within the microfluidic device, 2 μm fluorescent beads (excitation/emission: 488 nm/515 nm) (ThermoFisher) were suspended in water and perfused through the top channel using an OMI platform (Fluigent) at 1 μL min^{-1}. The channel had a square cross-section of 750 μm × 750 μm. Time-lapse fluorescence imaging was performed using an epifluorescence video-microscope Axio Observer Z1 (Zeiss), capturing sequences at a frame rate of 26 frames per second for 30 s. Image stacks were analyzed using the TrackMate plugin in Fiji (ImageJ).[22] Bead detection was performed using the LoG (Laplacian of Gaussian) detector, and tracks were generated using the Simple LAP tracker. Calibration of spatial and temporal resolution was applied prior to analysis, allowing automatic computation of bead displacement and instantaneous velocity. Final velocity distributions were extracted from the TrackMate results table and used to assess flow profile across the channel.

2.6 Cell culture

Caco-2 cells (clone TC-7) were obtained from Sansonetti's lab. Cells were grown in Dulbecco's modified Eagle medium (DMEM, Gibco) supplemented with 20% FBS (fetal bovine serum, Fisher Scientific, France) 100 U mL^{-1} penicillin, 100 mg mL^{-1} streptomycin and non-essential amino acid (Gibco) in 5% CO_2 at 37 °C.

2.7 Human gut-on-chip seeding and culture

The 3DP-μGut PDMS chips were coated overnight at 37 °C 5% CO_2 with type I collagen (ThermoFisher, USA) and Matrigel (Avantor, USA) diluted in Caco-2 culture medium at respectively 30 μg mL^{-1} and 100 μg mL^{-1}. The channels were rinsed with cell culture medium and cells seeded at 2.10^6 cells per mL in the upper channel for 4 hours at 37 °C 5% CO_2. After cell attachment, the top channel was gently washed using warm cell culture media. Chips were maintained statically overnight. For the chips under flow conditions, the top and/or the bottom were connected either to a microfluidic circuit actuated by Flow EZ pressure controllers (Fluigent, France), or an integrated and connected device OMI (Fluigent, France). They were cultured under 37 °C and 5% CO_2 conditions for 7 days as their static counterparts. The flow was set to 60 μL per hour. Cell culture media was renewed every 48 hours.

2.8 Live dead assay

Cell viability was assessed using the LIVE/DEAD™ Viability/Cytotoxicity Kit (ThermoFisher Scientific) according to the manufacturer's protocol. Briefly, a staining solution was

freshly prepared by diluting calcein-AM (2 μM final concentration) and ethidium homodimer-1 (4 μM final concentration) in PBS. 3DP-μGut were incubated with the staining solution for 40 minutes at 37 °C. Following incubation, 3DP-μGut were rinsed with Caco-2 medium and imaged using an epifluorescence video-microscope Axio Observer Z1 (Zeiss). Live cells were identified by green fluorescence (calcein-AM), while dead cells exhibited red fluorescence (ethidium homodimer-1). Quantification was performed by analyzing the 3DP-μGut images using ImageJ software. The percentage of viable cells was calculated as the ratio of calcein-positive cells to the total number of cells (calcein-positive + ethidium homodimer-positive).

2.9 RT-qPCR

3DP-μGut were maintained until day 7 and used. The channels were washed by injection of 100 μL DPBS +/+ into the channel inlets. A new empty 200 μL filtered tip was inserted to channel outlets. 100 μL RNA lysis buffer (RNeasy Plus Micro Kit, Qiagen) was injected into top channel for 5 minutes incubation time and followed by quickly pressing and releasing the micropipette plunger three times for homogenization and sampling. The procedure was repeated 3 times. The 300 μL of lysates were collected and stored at −80 °C for RNA analysis. Total RNA was isolated using the RNeasy Plus Micro Kit (Qiagen). 100–800 ng of total RNA was used for cDNA synthesis, using the high capacity cDNA reverse transcription kit (Applied Biosystems). Quantitative real-time PCR was performed using the Takyon™ Low Rox SYBR MasterMix dTTP Blue (Eurogentec). qPCR was performed on a QuantStudio 3 System (Applied Biosystems). Specific primers (Sigma-Aldrich) used for the qRT-PCR were listed in the following table (Table 2). Amplicons specificity was confirmed by melting-curve analysis. Relative RNA level was quantified using the ΔΔCt method and normalized to the endogenous control GAPDH.

2.10 Co-culture with gut commensal strain *Lactiplantibacillus plantarum* NCIMB8826

The *Lactiplantibacillus plantarum* NCIMB8826-mCherry strain used in our study was described previously.[23] Briefly, the *L. plantarum* codon-optimized mCherry cDNA under the control of P*ldh* (lactate dehydrogenase gene from *L. plantarum*) was cloned into a lactic acid bacteria expression vector (containing the chloramphenicol resistance gene) and the resulting construct was introduced into *L. plantarum* NCIMB8826 by electrotransformation. The fluorescent *L. plantarum* strain was grown at 37 °C in MRS medium (Difco, Becton Dickinson, Le Pont de Claix, France). Chloramphenicol (Sigma-Aldrich, St Quentin Fallavier, France) was added to culture media for bacterial selection at a final concentration of 10 μg mL^{-1}.

Prior to *L. plantarum* injection, the GOC were either matured for 7 days under flow conditions to ensure villi formation or kept under static conditions. The day before the medium was switched with Caco-2 cell culture media without penicillin and streptomycin in both channels. Then, the 3DP-μGut were disconnected from the flow circuit and the *L. plantarum* were introduced in the top channel at an inoculum of 20 000 CFU (colony-forming units). After two hours, the 3DP-μGut was reinserted and flow conditions were re-applied for 24 h on the apical channel. The *L. plantarum* were retrieved by cutting the 3DP-μGut in half and scratching the channel with a pipet tip, then vigorously pipetting 600 μL of PBS 0.1% Triton X-100. MRS agar supplemented with chloramphenicol was used as the selective medium to isolate and enumerate *L. plantarum*.

2.11 *Shigella* infection

3DP-μGut chips were washed overnight at a flow rate of 60 μL per hour with Caco-2 cell culture medium without penicillin in both channels. Subsequently, *S. flexneri* (M90T-GFP strain) was introduced into the top channel as described previously.[24] Briefly, the infection protocol was as follows: after a 2 hour exposure, the chips were washed twice by gravity flow using Caco-2 culture medium supplemented with gentamicin at a final concentration of 50 mg mL^{-1} (ThermoFisher). The chips were then incubated overnight. The infection was halted by gently flushing 4% paraformaldehyde (Electron Microscopy Sciences) diluted in PBS containing Ca^{2+} and Mg^{2+} (Gibco) through both the top and bottom channels.

2.12 Immunofluorescence

3DP-μGut were fixed in PBS, 4% paraformaldehyde for 30 min at room temperature, permeabilized in PBS, 0.5% BSA,

Table 2 List of primers used for the qRT-PCR

Gene name	Forward primer (5′ – 3′)	Reverse primer (5′ – 3′)
GAPDH	GTCTCCTCTGACTTCAACAGCG	ACCACCCTGTTGCTGTAGCCAA
TJP1	GTCCAGAATCTCGGAAAAGTGCC	CTTTCAGCGCACCATACCAACC
OCLN	ATGGCAAAGTGAATGACAAGCGG	CTGTAACGAGGCTGCCTGAAGT
CLDN1	GTCTTTGACTCCTTGCTGAATCTG	CACCTCATCGTCTTCCAAGCAC
CDH1	GCCTCCTGAAAAGAGAGTGGAAG	TGGCAGTGTCTCTCCAAATCCG
VIL1	GCTGCTCTACACCTACCTCATC	TTCTGGTCCAGGATGACGGCTT
ALPI	CATACCTGGCTCTGTCCAAGA	GTCTGGAAGTTGGCCTTGAC
CD24	CACGCAGATTTATTCCAGTGAAAC	GACCACGAAGAGACTGGCTGTT
MUC1	CCTACCATCCTATGAGCGAGTAC	GCTGGGTTTGTGTAAGAGAGGC
MUC2	ACTCTCCACACCCAGCATCATC	GTGTCTCCGTATGTGCCGTTGT

0.2% Triton-X100 (Sigma-Aldrich) for 15 min at room temperature and blocked in PBS, 5% BSA (Sigma-Aldrich) and 2% FBS (Fisher Scientific, France) for 1 h at room temperature. GoC were then incubated with the primary antibody in PBS, 0.5% BSA, 0.2% Triton-X100 (Sigma-Aldrich) for 2 h at room temperature, rinsed 2 times for 5 min with PBS and incubated for 1 h at room temperature with the secondary antibody in PBS, 0.5% BSA, 0.2% Triton-X100 and rinsed as above. GoC were incubated in PBS, 1 μg mL^{-1} DAPI (Thermofisher, USA) for 20 min at room temperature, rinsed twice for 5 min with PBS and stored at 4 °C until observation. The antibody primary and secondary antibody were listed in the following table (Table 3).

For transversal sections, 3DP-μGut chips were embedded in thick agarose gel 5% and cut with Compresstome® VF-310-0Z (Precisionary Instruments) in 400 μm thin segments. The slices were preserved and mounted with PBS on glass coverslip prior to imaging.

2.13 Microscopy

Vertical slices of the empty gut chip were imaged under a video-microscope Axio Observer Z1 equipped with a Prime95B camera (Zeiss). The maturation of the 3DP-μGut was followed by phase contrast imaging with an Eclipse TS2 inverted microscope (Nikon). Fluorescence images were taken using a spinning disk microscope equipped with a CSU-W1confocal scanner unit (Nikon) and objectives 10× CFI Plan Fluor (ON0.30), 20× CFI Plan Apo Lambda (ON0.75), 40× CFI Plan Apo (ON0.95). Images were adjusted for brightness, color balance, and/or contrast uniformly across all pixels, as necessary, in ImageJ (v1.46r, National Institutes of Health).[25]

2.14 Permeability assay

After 7 days of culture, FITC–dextran 70 kDa was injected to the top channel, 10 μg mL^{-1} in cell culture media. Empty 3DP-μGut were used as a control. After overnight incubation at 37 °C and 5% CO_2, samples from the top and bottom were collected and stored in the dark at 4 °C upon measurement.

Table 3 List of antibodies used for immunofluorescence staining

Antigen	Dilution	Catalogue #	Isotype	Manufacturer
Primary antibody				
CD324 (E-cadherin)	1/50	610182	Mousse	BD biosciences
Villin 1	1/100	13463197	Rabbit	ThermoFisher
ZO-1	1/100	61-7300	Rabbit	ThermoFisher
Secondary antibody				
Alexa 488	1/1000	A32790	Donkey anti rabbit	ThermoFisher
Alexa 568	1/1000	A10042	Donkey anti rabbit	ThermoFisher
Alexa 568	1/1000	A11004	Goat anti mouse	ThermoFisher
Other				
Phalloidin Alexa 488	1/400	A12379		ThermoFisher
Phalloidin Alexa 568	1/400	A22283		ThermoFisher
Phalloidin Alexa 647	1/400	A22287		ThermoFisher

Fluorescence levels were measured in a VictorX3 multilabel plate reader (PerkinElmer, USA) with excitation wavelength of 485–414 nm and an emission wavelength of 535–525 nm. The apparent permeability coefficient (Papp) was calculated based on the final fluorescence values using the following simplified formula:

$$\text{Papp} = \frac{I_{\text{bottom}}}{I_{\text{top}} \times A \times t}$$

where I_{bottom} and I_{top} are the fluorescence intensities measured at the end of the experiment in the top and bottom channels, respectively, A is the surface area of the permeable membrane (cm^2), and t is the incubation time (s). This approach assumes a linear transfer of dextran during the incubation period.

3 Results

3.1 SLA 3D-printing produces robust and reproductible molds for PDMS casting

The overall 3DP-μGut design consists of two channels separated by a porous membrane following a modified curved channels geometry replicating the intricacy of the human intestine and its physiodynamics.[20,26] To optimize chip production, molds were created by pairs, one for the bottom channel of the chip (blue, Fig. 1A) and one for the top channel (Red, Fig. 1A). Each mold is composed of nine identical micropatterns (Fig. 1D, E, F), respectively 200 μm and 750 μm high. The design integrates pillars of 1.2 mm diameter for the inlets and outlets access to avoid fastidious manual punching and its associated variability. To confirm that the resulting shear stress is in physiological scale, the medium flow inside the device was numerically modelled (Fig. 1B) and validated experimentally by measuring the local velocities. The simulated shear stress is distributed across the channel, perpendicularly to the flow direction, ranging from 1 to 10.10–4 Pa (0.001 to 0.01 dyne per cm^2). The measured velocity (Fig. 1C) ranged from a minimum of 20 μm s^{-1} near the channel wall to a maximum of 120 μm s^{-1} at the center, corresponding to wall shear stress values between 2.13×10^{-4} Pa and 12.8×10^{-4} Pa, which is slightly higher than the simulation results.

The master molds were then fabricated using a commercial desktop SLA printer (Form 3, Formlabs). The printed pieces were then pros-treated. Briefly, they were rinsed with isopropanol, post cured under UV and silanized to ensure quick demolding and preventing stickiness of the PDMS to the resin molds. In comparison to the conventional microfabrication techniques with soft lithography, this 3D printing-based fabrication protocol takes less than a day, can be easily implemented in a biology lab and is cost effective (Table S1†).

We validated the 3D printing technique as a robust alternative for mold fabrication by analyzing the reproducibility and resolution of the fabricated structures.

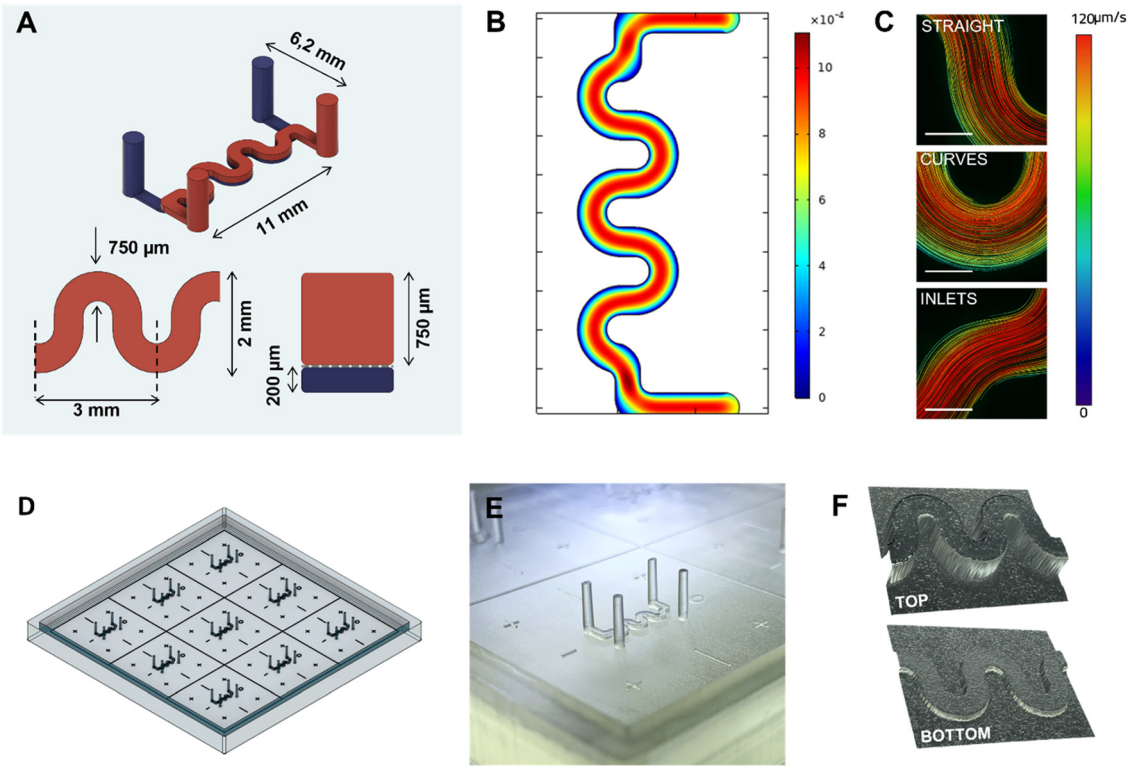

Fig. 1 Design, simulation and fabrication process of the 3D printed mold. A) Schematical view of the microfluidic channels. From top left to bottom right: 3D view, top view, vertical cross-section. The TOP channel is in red and the bottom channel in blue. B) Simulated shear stress inside the chip geometry, the results are expressed in Pa. C) Measured velocities of fluorescent beads inside the microfluidic channel. D) CAD model of the 3DP-µGut mold, bar = 500 µm E) close up photo of one of the printed patterns for a TOP mold. F) 3D reconstitution of the printed patterns imaged with a surfaced microscope.

Comparison between the CAD design and the printed molds by SLA 3D printer (FORM 3) and MSLA 3D printer (FORM 4) (Fig. S2A†) demonstrated high structural fidelity. Minor deviations observed at the microscale for both printers were within acceptable tolerances for the biggest structures (500 µm) and did not impact the function of the resulting gut-on-chip device. The MSLA 3D printing technique provide better accuracy in terms of dimensions and structure fidelity (Fig. S2C†). These results confirm that 3D printing offers a reliable and accessible approach for producing complex, biomimetic topographies.

Surface roughness of 3D-printed molds using various resins and printer models was assessed by AFM on PDMS replicas molded from SU-8, polystyrene Petri dishes, micromachined aluminum (from a previous study ref. 5), and 3D-printed molds (Fig. 2A). Among the printed molds, Form 4 with Clear V5 resin yielded the lowest roughness (R_a = 17 nm, R_q = 22 nm), approaching that of the silicon wafer reference (R_a = 14 nm, R_q = 10 nm). In contrast, Form 3 with Clear V4 showed significantly higher values (R_a = 435 nm, R_q = 526 nm), similar to roughness reported in prior work.[27] The Rigid 4000 resin also resulted in rough surfaces (R_a = 367 nm, R_q = 463 nm), while Black V5 and Precision V1 resins gave intermediate results. Aluminum molds showed moderate roughness (R_a = 186 nm), whereas Petri dishes had the smoothest surfaces (R_a = 1.2 nm, R_q = 2.2 nm). These results highlight the critical influence of printer model and resin on mold quality, with Form 4–Clear V5 as the best-performing combination.

A direct comparison of Form 3 and Form 4 with Clear resins confirmed improved surface quality with the newer printer (Fig. S2B, Table S2†). At 25 µm resolution, Form 4 achieved R_a = 106 nm *versus* 1054 nm for Form 3. Even at 100 µm, Form 4 outperformed Form 3, reaching R_a = 30 nm compared to 378 nm. Notably, Form 4 exhibited a consistent inverse relationship between layer thickness and roughness, unlike Form 3, where thinner layers did not always yield smoother surfaces. The best results were achieved at 100 µm, with surface metrics approaching those of microfabricated references. Despite the overall improvements, residual surface patterns—typically circular or striated—were observed on Form 4–Clear V5 prints (Fig. S2C†). These artifacts, inherent to the layer-by-layer stereolithography process, were more visible at finer resolutions (25 µm) and less pronounced at 100 µm. While they did not impair the mold's functional performance, such features could influence optical clarity or micro-topographical consistency in sensitive applications (Fig. S2E†) (Table 4).

Molds were then further characterized by measuring the height of the patterns for the bottom and the top mold with a high-resolution digital microscope (Fig. 2B). Measurements show a low variability between the patterns from the same

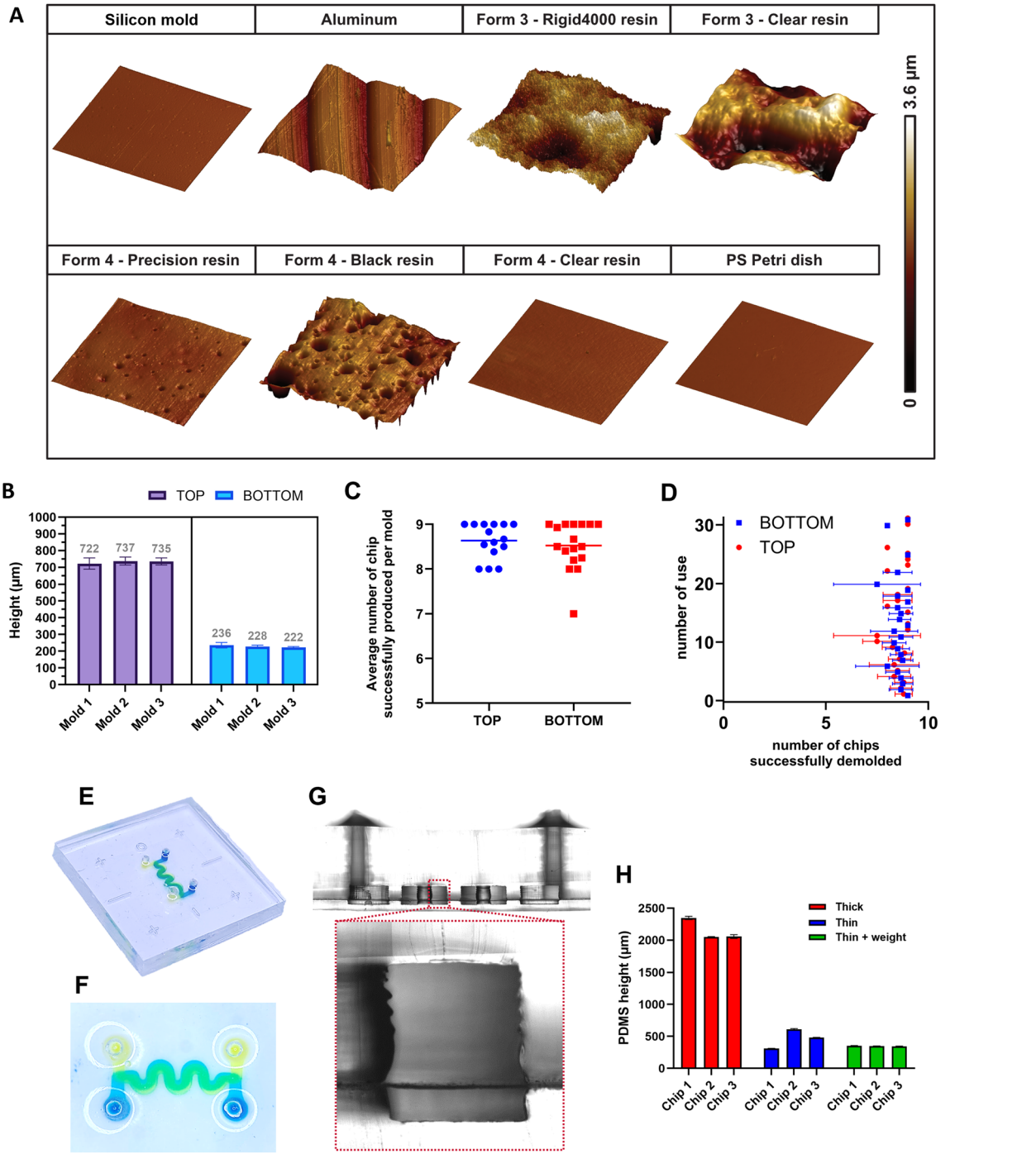

Fig. 2 3D printed mold characterization. A) Topography of PDMS slabs casted on either a silicon mold, PS Petri dish, micromachined aluminum mold or 3D printed molds. Scan size: 100 μm^2 B) channel height measurements within the same mold of between different batches. C) Graph of the average number of chips produced per molds, one point is one iteration. D) Evaluation of the performance of the molds across time. E) and F) Views of the final 3DP-µGut device, top channel in yellow and bottom channel in blue. G) Cross section of the resulting PDMS chip. H) Thickness measurement of the PDMS layer under the BOTTOM channel depending on molding techniques.

mold with $meanSEM_{Top}$ = 4.4 µm and $meanSEM_{Bottom}$ = 1.74 µm, and reproducibility between different molds with SD_{Top} = 15.3 µm and SD_{Bottom} = 7.4 µm from one mold to the other.

Next, we assessed the durability of molds. To do so, we followed the performances of each mold individually for 3DPuGut fabrication. The results show an average successful demolding superior to eight individual chips for the wide majority of the produced molds (Fig. 2C). Interestingly, the top and the bottom molds provide a continuous high rate of successful demolding even after thirty uses, proving the robustness of the 3D printing technique to fabricate microfluidic molds (Fig. 2D). However, the successive PDMS

Table 4 Rugosity measurement for PDMS parts casted on silicon wafer mold, PS Petri dish, micromachined aluminum mold and 3D printed molds

Molds	Resin	Rugosity	
		R_a (nm)	R_q (nm)
3D printed FORM 3	Rigid 4000	367	463
	Clear V4	435	526
3D printed FORM 4	Clear V5	17	22
	Black V5	286	410
	Precision V1	52	70
Si wafer		14	10
Micromachined aluminium		186	221
PS Petri dish		1.2	2.2

curing at 65 °C appeared to have a deforming effect on the 3D printed pieces (Fig. S1A†) with a light incurvation of the mold base. To prevent this deformation and improving molds longevity, weights were added on top of the molds during PDMS curing.

3.2 PDMS chip assembly and optimization for high resolution imaging

PDMS was cast onto the 3D printed pieces to fabricate the 3DP-μGut devices. After demolding, the PDMS slabs were cut in individual half gut chips. Top and bottom parts were then assembled together with a PET membrane in between thanks to surface treatment with APTES, plasma exposure and contact bonding. The resulting 3DP-μGut is presented in Fig. 2E and F. On the vertical cut of the chip (Fig. 2G), we can observe a good curing and faithful reproduction of the design geometry with sharp angles. Some undulations are visible on the sides of the top channels due to the layer processing of the 3D printer and its resolution in Z (25 μm). PDMS was molded on a new or an old (>25 uses) mold to challenge the durability of the 3D printed structures. The results are shown in Fig. S1B† with no visible alterations of the mold.

Additionally, in order to optimize the devices for high resolution imaging we needed the thinnest layer of PDMS as possible on the bottom side. To achieve sub-millimeter thickness, the liquid PDMS was mechanically pressed against the bottom mold with a PC flat square and thermally cured with a weight on top to ensure a controlled height. Fig. 2H shows the differences in height measured depending on the molding technique, no press, pressed without weight and pressed with weight. The plastic lid combined with the weight appears to be the best method to achieve both very low thickness around 300 μm and repeatability.

3.3 Caco-2 differentiate in villi-like architectures inside the 3DP-μGut

To validate the biocompatibility of our 3DP-μGut devices with intestinal cells we coated and seeded Caco-2 cells inside the top channel. Using live/dead assay, we did not observe significant cytotoxic cell death within 24 h, 8 days or 15 days of culture (Fig. S3†). The devices were then connected to a flow circuit with microfluidic pumps and a continuous flow of medium at 60 μL h^{-1} was applied. We followed the maturation of the epithelium under phase contrast microscopy. Fig. 3 shows the change in the structuration of cells and morphology under the effect of physiological flow.

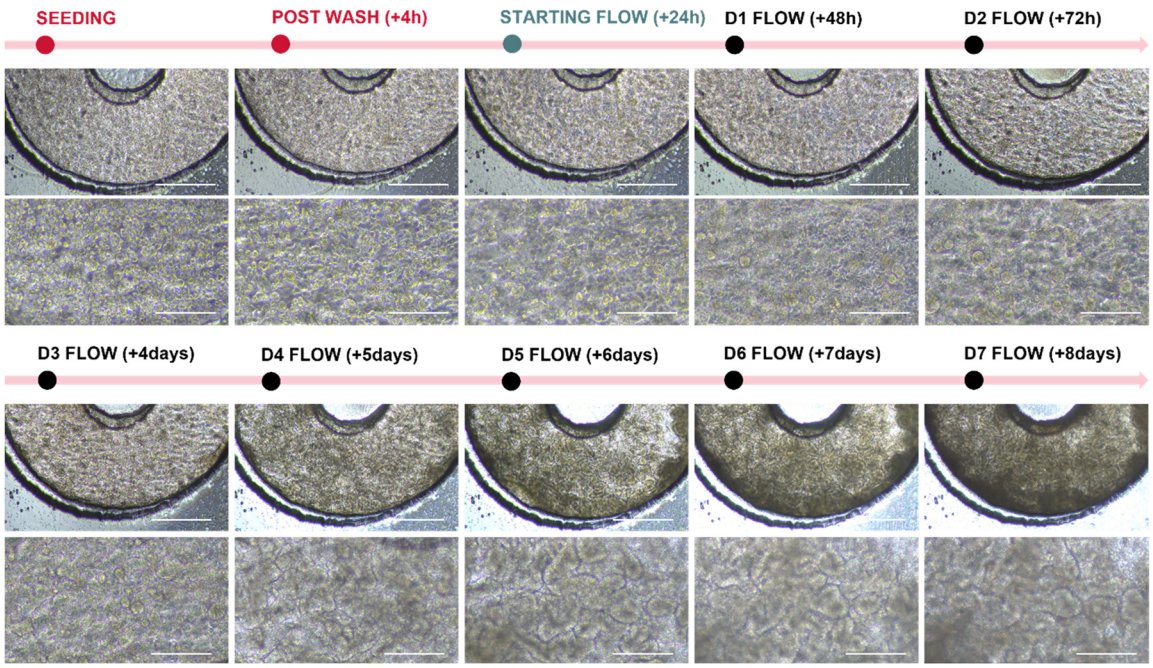

Fig. 3 3DP-μGut maturation. Phase contrast imaging of the Caco-2 maturation inside the 3DP-μGut devices during one week under flow conditions, n = 4. Top images: bar = 500 μm, bottom images: bar = 250 μm.

The Caco-2 differentiated from a cell monolayer after one day into a 3D invaginated micro architecture on day 7. As a control, cells were kept under static conditions and no structuration of the epithelium in 3D was observed at day 7 (Fig. S4A†).

To confirm further these structural observations, we embedded 3DP-μGut into agar, crosscut 400 μm sections and performed immunostaining. As observed previously, Caco-2 cells remain organized in a flat monolayer under static conditions, while villi-like structures are observed under continuous flow exposure (Fig. 4A and B). Furthermore, the impact of the basal *versus* apical flow was investigated (Fig. S4B†). We observed that the basal flow is sufficient and necessary to achieve such cell organization, in contrary to the apical flow which is not sufficient by itself for a complete structuration, which is consistent with anterior studies.[21]

The functionality of the intestinal epithelium was assessed using immunofluorescence staining, revealing the expression of the tight junction protein ZO-1 (Fig. 4C). To further validate the establishment and maturation of the epithelial barrier, the integrity of tight and adherens junctions was quantitatively analyzed at multiple time points—4 hours post-seeding, 24 hours, and 72 hours (+24 h under flow conditions). These analyses confirmed the progressive formation of a continuous and functional intestinal barrier (Fig. S5A–C†). To assess the polarization and the differentiation of the Caco-2 cells the villin was also marked. As expected, the 3DP-μGut clearly expresses villin in higher concentration at the luminal side (Fig. 4C). The epithelial permeability was observed by measuring transport of 70 kDa FITC–dextran across the cell barrier. The results show a strong decrease in permeability between empty control chip and colonized 3DP-μGuts indicating an effective barrier after seven days in culture in either static or flow conditions (Fig. 4D). The measured values of Papp are in range similar to commercially available gut-on-chip models.[24,28,29] The expression of epithelial junctional markers confirmed the functional integrity of the epithelium within the 3DP-μGut model (Fig. S5D†), consistent with previously reported findings.[30]

3.4 Automation of the 3DP-μGut cell culture with a plug and play microfluidic platform

One of the bottlenecks for a wider adoption of OoC is the complexity of the microfluidic instrumentation. Keeping the circuit sterile while performing live imaging can indeed be a struggle with conventional microfluidic pumps, requiring disconnecting the chips from the fluidic circuit. To prove the adaptability of the 3DP-μGut device, we automated the culture of the Caco-2 with OMI platforms, which provide an all-in-one solution for chip perfusion (Fig. S6†).

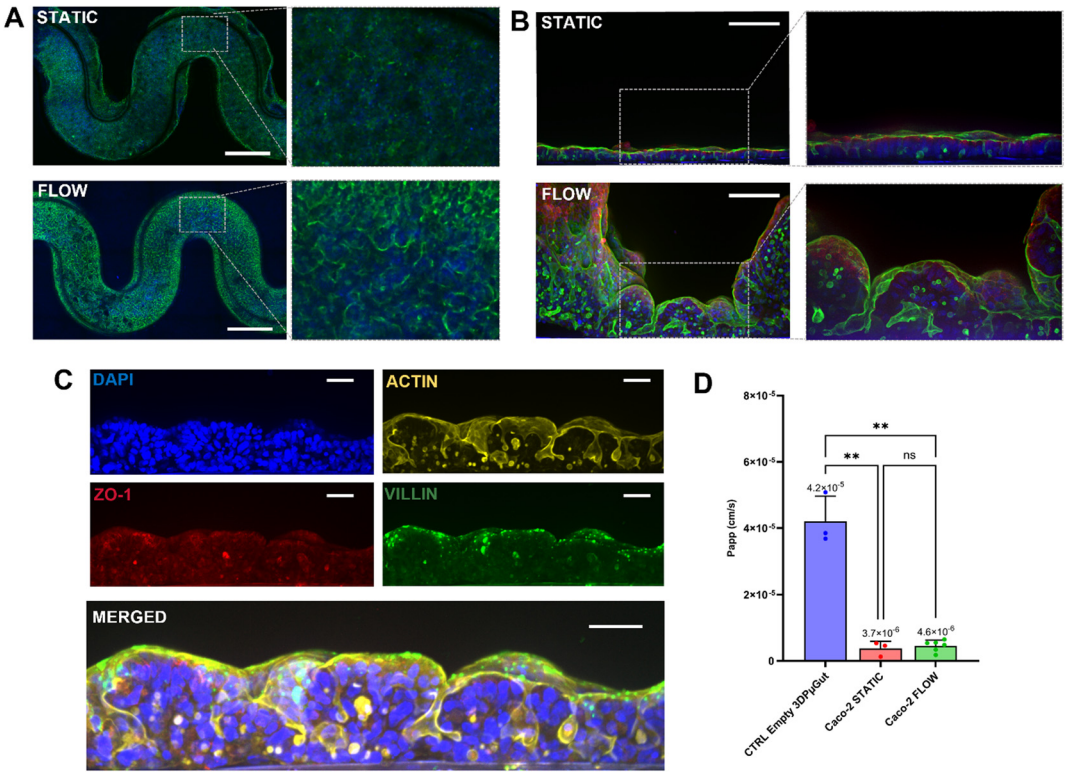

Fig. 4 3DP-μGut 3D structuration. A)–C) immunofluorescence staining of the Caco-2 cells inside the 3DP-μGut devices. n = 3 A) top view, nucleus in blue (DAPI and actin in green, bar = 750 μm B) cross-section view, nucleus in blue (DAPI), tight junctions (ZO-1) in red and actin in green, bar = 100 μm C) cross-section view, nucleus in blue (DAPI), tight junctions (ZO-1) in red, villin in green and actin in yellow, bar = 50 μm. D) and E) Permeability assay inside the 3DP-μGut devices in static or flow conditions, $n \geq 3$.

The 3DP-μGuts were cultured under the automated setup following the same protocol of 60 μL h^{-1} flow for seven days with medium recirculation. Fresh medium was introduced every 3 days. The automized protocol and instrumentation resulted in the same self-organization of the Caco-2 cells in 3D microarchitecture (Fig. 5A and B) exhibiting villi-like structure higher than 100 μm, similar to what was obtained with conventional pneumatic microfluidic pumps (Fig. 5C). These results display the integration and automation potential for the 3DP-μGut and its future applications.

3.5 Role of epithelial cells 3D structuration's in host–bacteria interactions

The establishment of a differentiated, three-dimensional (3D) intestinal epithelium within 3DP-μGut proved critical for successful co-culture with the human commensal strain *L. plantarum* NCIMB8826. As shown previously, epithelial cells cultured under dynamic flow formed villus-like structures, while, in contrast, Caco-2 cultured in static conditions remained in a monolayer. Co-culture with *L. plantarum* in the 3D-differentiated system led to stable bacterial colonization (Fig. 6A), whereas in poorly structured monolayers, a progressive washout of the bacteria was observed under a flow rate of 1 μL min^{-1} (Fig. 6C and D). At the velocities encountered by the bacteria (Fig. 1C), such washout is consistent with findings reported for flat environments.[31] Villus-like topography not only increase the available surface area for bacterial adhesion compared to flat 2D monolayers, but also generate protective niches with reduced shear stress,[32] allowing bacteria to persist with a lower risk of being dislodged.[33]

Additionally, in the 3DP-μGut model, we observed a significantly higher rate of *Shigella* infection in the 3D-structured epithelium compared to the flat monolayer configuration (Fig. 6B and E). The 3D architecture, which better mimics the villus-like topography of the intestinal epithelium, appeared to enhance bacterial adhesion and invasion. Quantitative analysis showed increased bacterial load and more widespread epithelial invasion in the 3D and low velocity regions, suggesting that the physical microenvironment plays a key role in facilitating *Shigella* pathogenesis.[24] These findings highlight the necessity of biomimetic 3D structuration and cellular differentiation to recapitulate host–microbe interactions observed *in vivo* and to maintain a physiologically relevant and stable co-culture environment.

4 Discussion

This study demonstrated the effectiveness of SLA 3D printing for the fabrication of molds used in the production of gut-on-chip devices: the 3DP-μGuts. The printed molds exhibit high resolution, sufficiently for reproducing cell culture microchannels. Unlike traditional photolithography, SLA 3D printing offers increased flexibility in mold design and customization, especially regarding achievable high aspect ratio.[34] They can be manufactured more quickly and at lower cost, while maintaining adequate accuracy for biological applications. The fabrication of the 3DP-μGuts does not require an extensive training or dedicated facilities, allowing its rapid implementation in non-specialized labs.[35]

The versatility of this method allows the channel designs to be tailored for a wide range of applications and even for other organ-on-chip systems such as lungs,[14] breast,[19] or blood vessels,[36] with similar size requirements. The structural details of the 3D-printed molds depend on the resolution of the selected printer. While the manufacturer specifies an approximate resolution of 100 μm in the *XY* plane, other studies have reported the successful fabrication of 25 μm features using the same general-purpose desktop SLA printer.[37] Using our set-up, the accuracy of printing resolution falls around 250 μm (up to 100 μm in *XY*), which is compatible with the dimensional requirement for many

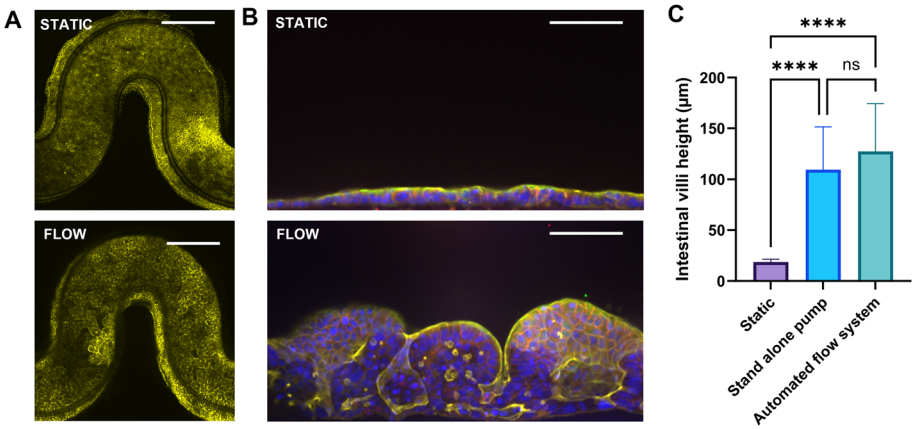

Fig. 5 3DP-μGut cell culture automation with plug and play microfluidic platform. A) and B) Immunofluorescence staining of the Caco-2 cells inside the 3DP-μGut devices under static or flow conditions. *n* = 2 A) top view, actin in yellow bar = 750 μm B) cross section view, nucleus in blue (DAPI), adherent junctions (E-cadherin) in red and actin in yellow, bar = 100 μm. C) Villi height measurement between static and flow conditions with stand-alone pumps or plug and play systems.

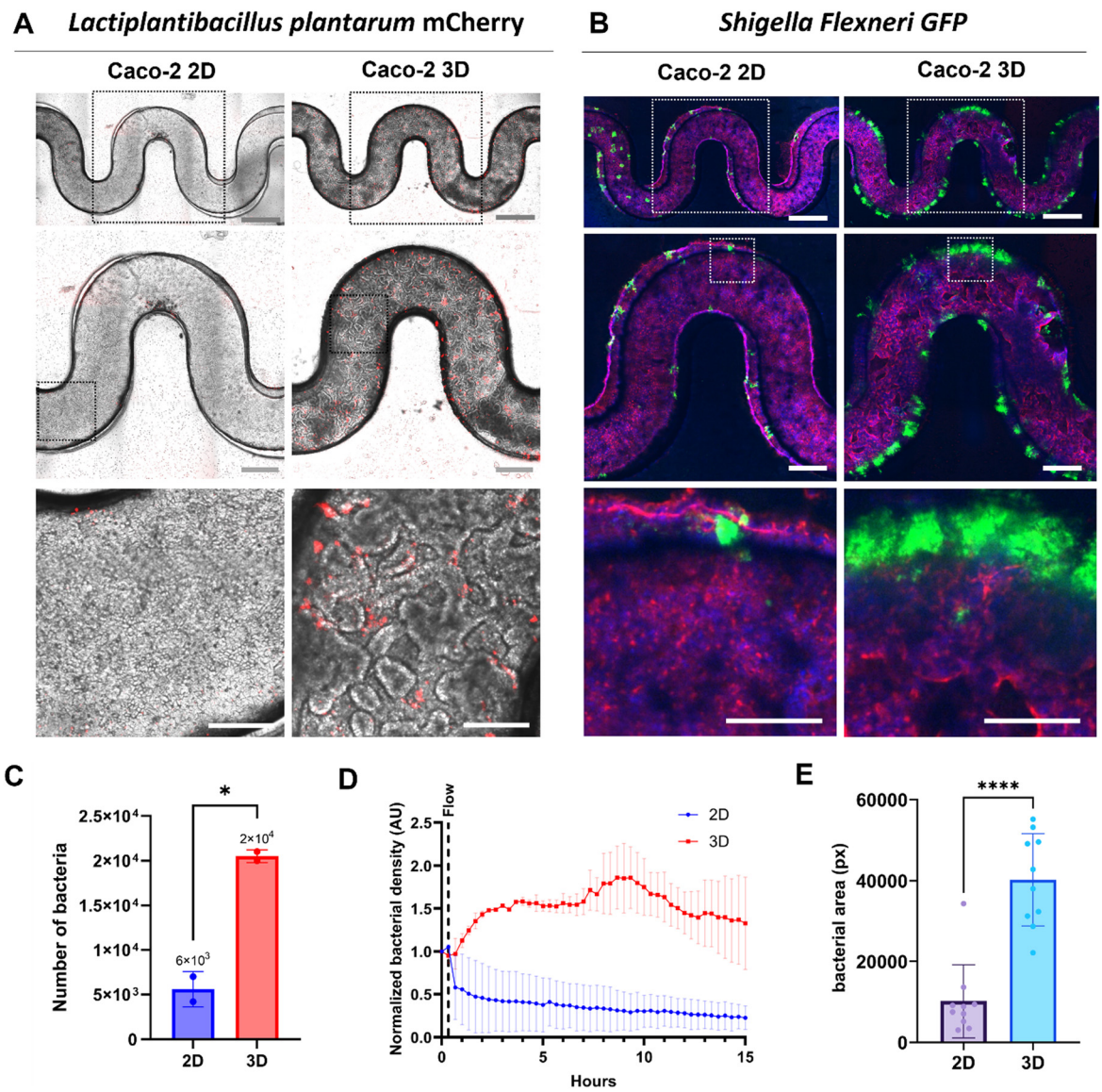

Fig. 6 3DP-μGut co culture with gut commensal strain and infection with pathogenic bacteria. A) Cocultue of Caco-2 cells with *L. plantarum* NCIMB8826 (inoculum 20 000 CFU) after 24 h. cells in grey (phase contrast) and bacteria in red. Bar = 1 mm (top), 500 μm (middle), 200 μm (bottom) B) *Shigella flexneri* (green) infection (MOI = 1); nuclei (DAPI) in blue and actin in red. Bar = 1 mm (top), 500 μm (middle), 200 μm (bottom) C) *L. plantarum* count after retrieval from the 3DP-μGut. k = 2 D) normalized *L. plantarum* density inside the 3DP-μGut over time k = 2 E) *Shigella flexneri* bacterial area after infection. n = 5, k = 2.

OoC design. More resolutive 3D printing technologies already exist and achieve resolution of 2 μm (ref. 38) or even lower at the nanometer scale.[39] However, these high-end printers are typically costly, require specialized training, and are often limited by smaller build volumes, making them less accessible for routine prototyping in academic labs. The selection of a widely available desktop SLA printer in this study reflects a practical compromise between resolution, accessibility, and production scale.

To provide an easy and accessible OoC platform, PDMS was selected as pragmatic OoC material as it is widely available, easy-to-use and well characterized. To date, PDMS remains a gold standard material in microfluidics due to its biocompatibility, oxygen permeability, and optical transparency, critical features for long-term epithelial cell culture and live imaging. While this material remains extensively used for OoC, there is a rising concern as PDMS is known to adsorb small hydrophobic molecules and its usage should be carefully considered upon the applications.[40] Although PDMS casting inherently limits the throughput of microfluidic chip production, as compared to direct 3D-printed OoC, resin biocompatibility and/or design capacities remains a major issue in direct printing strategy. Here, the integration with 3D-printed molds enhances manufacturing scalability. The optimized molds developed in this study allow the simultaneous production of fifteen 3DP-μGuts per batch. Furthermore, inlet and outlet access ports were integrated directly into the mold design, eliminating the

need for time-consuming manual punching. The rapid fabrication of molds facilitates their multiplication and enables parallelized production of 3DP-μGuts, further improving efficiency. 3D-printed molds have also recently proven compatible with higher-throughput fabrication methods such as hot embossing,[41] suggesting that the technique could be scaled even further for industrial applications. However, at this stage, 3DμGUT is currently designed for low/mid throughput functional assays. The integration in higher throughput workflow would inherently requires new chip design, compatible with further scaling. However, the modular design of 3DμGUT might facilitate its integration with standard imaging platform and semi-automated workflow, paving the way toward multi-organ on chip system compatibility in future development.

Mold durability and surface characteristics are also important considerations. The repeated casting of PDMS can lead to wear of the resin molds, particularly under high-temperature curing conditions. However, the robust photopolymer resins used in SLA printing—especially those with high thermal resistance—provide sufficient durability for multiple casting cycles before deterioration occurs. Surface roughness, inherent to the layer-by-layer nature of SLA printing, could influence the fidelity of microchannel replication and potentially affect PDMS demolding and subsequent cell behavior. Post-processing recipes[42] and techniques have been proposed such as resin polishing or surface coating[43] can mitigate these issues and ensure reproducible surface quality. In this study, we successfully fabricated durable molds with remarkably low surface roughness, approaching that of silicon wafers, achieved directly from the SLA printing process without the need for complex surface treatments.

Another approach consists in using the advantages of SLA manufacturing by printing the microfluidic devices directly with a bio compatible resin. Although, it remains challenging in terms of optical transparency, leakage management, cell adhesion and cytotoxicity.[9] A Biocompatible PEGDA has been used to print transparent bio-microfluidic devices.[44] The layer by layer printing could also pave the way to *in situ* 3D structuration of hydrogels inside the printed microfluidic channels[45] for instance to recreate intestinal structures, similar to the gut-on-chip proposed by Nikolaev and colleagues.[46]

The potential of the 3DP-μGut platform extends beyond basic epithelial models. Caco-2 cells were used here as a proof of concept due to their well-established use in modeling intestinal barrier function and differentiation. However, more physiologically relevant cell sources, including human induced pluripotent stem cells (hiPSCs), or patient-derived organoids, could enhance the complexity and clinical relevance of the model. These advanced cell sources allow for the recapitulation of individual patient phenotypes and disease states, thereby supporting the development of personalized gut-on-chip systems.[47,48] Here, we also demonstrated that our GoC is readily useful for applications in microbiology thanks to its capacity for co-culturing and monitoring the spatio-temporal dynamics in real-time human commensal bacteria colonization and growth at the intestinal interface. In addition, we demonstrated the physiological relevance of the model by successfully infecting a human restricted pathogen, where most of the small animal models are inefficient.[49] Thus, this model could pave its way in many labs dissecting host–microbe interactions, probiotic and evaluation of therapeutics against human restricted pathogen.[50] In addition, the flexible and adjustable design of the 3D printed mold facilitates the testing of various intestinal microenvironment configurations. Coupled together, they could pave the way to patient-gut-on-chips and personalized medicine.[51] Additionally, the ability to fabricate customized molds could open the possibility of modeling intestinal architectures specific to certain pathologies, offering new avenues for disease modeling and therapeutic development.

5 Conclusion

Here we described the fabrication process of the 3DP-μGut devices with 3D printed molds. We assessed the reproducibility of the method and characterized the surface and the longevity of the produced molds. We evaluated the assembly of the final devices and tested their biocompatibility by cultivating Caco-2 cells inside the 3DP-μGuts. The cells exhibited spontaneous 3D structuring in villi-like morphology under flow conditions. They displayed typical enterocytes maturation markers and formed an effective epithelial barrier. Finally, we show the integrability of the 3DP-μGut within a plug and play fluidic system. Through this work we emphasize the potential for SLA 3D printing in being a promising technology for the fabrication of molds for intestinal-on-chip devices. Its advantages in terms of precision and design flexibility allow pushing the limits of *in vitro* models.

Data availability

The authors confirm that the data supporting the findings of this study are available within the article and as its ESI.†

Author contributions

E. D. designed, performed and analyzed most of the experiments and wrote the manuscript. A. B. fabricated the microfluidic chips and participated in the Caco-2 cells culture. S. J. performed AFM experiments. N. D. performed the qPCR experiment. S. P. and C. D. cultured the *Lactiplantibacillus* strain. C. D. copyedited the manuscript. A. G. led the work, participated in its funding, in design and analysis of most experiments, and wrote the manuscript with E. D.

Conflicts of interest

A. G. is a Fluigent ambassador. The other authors declare no conflict of interest.

Acknowledgements

The authors would like to thank Fluigent for the lending of two OMI platforms. We also thank Sophie Salomé-Desnoulez from BICeL – US 41 – UAR 2014 – PLBS for her guidance on microcopy protocols. We also thank Jerome Vicogne from the Center of Infection and Immunity of Lille for granting us the access to the Keyence microscope. We would also like to thank Fabrice Soncin from CNRS/IIS/Centre Oscar Lambret/Lille University SMMiL-E Project for the access to the COMSOL software. We also thank members of MoHMI team for comments and discussion on the manuscript. This research is supported by Atip-Avenir funding, MEL "Accueil de talents" funding, GIS FC3R with fundings managed by Inserm for the project R23048ES and region Hauts de France "Start Airr". The French government under the France-2030 program, the University of Lille and the Lille European Metropolis (MEL) are thanked for their funding and support for the project R-CDP-24-007-MOSAIC granted to AG.

References

1 J. M. Donkers, H. Eslami Amirabadi and E. van de Steeg, Intestine-on-a-chip: Next level *in vitro* research model of the human intestine, *Curr. Opin. Toxicol.*, 2021, **25**, 6–14.
2 S. N. Bhatia and D. E. Ingber, Microfluidic organs-on-chips, *Nat. Biotechnol.*, 2014, **32**(8), 760–772.
3 D. C. Duffy, J. C. McDonald, O. J. A. Schueller and G. M. Whitesides, Rapid Prototyping of Microfluidic Systems in Poly(dimethylsiloxane), *Anal. Chem.*, 1998, **70**(23), 4974–4984.
4 C. M. Yousuff, M. Danish, E. T. W. Ho, I. H. Kamal Basha and N. H. B. Hamid, Study on the Optimum Cutting Parameters of an Aluminum Mold for Effective Bonding Strength of a PDMS Microfluidic Device, *Micromachines*, 2017, **8**(8), 258.
5 E. Delannoy, G. Tellier, J. Cholet, A. M. Leroy, A. Treizebré and F. Soncin, Multi-Layered Human Blood Vessels-on-Chip Design Using Double Viscous Finger Patterning, *Biomedicines*, 2022, **10**(4), 797.
6 D. Carugo, J. Y. Lee, A. Pora, R. J. Browning, L. Capretto and C. Nastruzzi, *et al.*, Facile and cost-effective production of microscale PDMS architectures using a combined micromilling-replica moulding (μMi-REM) technique, *Biomed. Microdevices*, 2016, **18**(1), 4.
7 R. Suriano, A. Kuznetsov, S. M. Eaton, R. Kiyan, G. Cerullo and R. Osellame, *et al.*, Femtosecond laser ablation of polymeric substrates for the fabrication of microfluidic channels, *Appl. Surf. Sci.*, 2011, **257**(14), 6243–6250.
8 K. Liu, J. Xiang, Z. Ai, S. Zhang, Y. Fang and T. Chen, *et al.*, PMMA microfluidic chip fabrication using laser ablation and low temperature bonding with OCA film and LOCA, *Microsyst. Technol.*, 2017, **23**(6), 1937–1942.
9 N. Bhattacharjee, A. Urrios, S. Kang and A. Folch, The upcoming 3D-printing revolution in microfluidics, *Lab Chip*, 2016, **16**(10), 1720–1742.
10 L. A. Milton, M. S. Viglione, L. J. Y. Ong, G. P. Nordin and Y. C. Toh, Vat photopolymerization 3D printed microfluidic devices for organ-on-a-chip applications, *Lab Chip*, 2023, **23**(16), 3537–3560.
11 X. Wu, W. Shi, X. Liu and Z. Gu, Recent advances in 3D-printing-based organ-on-a-chip, *Eng. Med.*, 2024, **1**(1), 100003.
12 N. P. Macdonald, J. M. Cabot, P. Smejkal, R. M. Guijt, B. Paull and M. C. Breadmore, Comparing Microfluidic Performance of Three-Dimensional (3D) Printing Platforms, *Anal. Chem.*, 2017, **89**(7), 3858–3866.
13 H. Shafique, V. Karamzadeh, G. Kim, M. L. Shen, Y. Morocz and A. Sohrabi-Kashani, *et al.*, High-resolution low-cost LCD 3D printing for microfluidics and organ-on-a-chip devices, *Lab Chip*, 2024, **24**(10), 2774–2790.
14 J. Shrestha, M. Ghadiri, M. Shanmugavel, S. Razavi Bazaz, S. Vasilescu and L. Ding, *et al.*, A rapidly prototyped lung-on-a-chip model using 3D-printed molds, *Organs-on-a-Chip*, 2019, **1**, 100001.
15 T. E. Park, N. Mustafaoglu, A. Herland, R. Hasselkus, R. Mannix and E. A. FitzGerald, *et al.*, Hypoxia-enhanced Blood-Brain Barrier Chip recapitulates human barrier function and shuttling of drugs and antibodies, *Nat. Commun.*, 2019, **10**(1), 2621.
16 R. Novak, M. Didier, E. Calamari, C. F. Ng, Y. Choe and S. L. Clauson, *et al.*, Scalable Fabrication of Stretchable, Dual Channel, Microfluidic Organ Chips, *J. Visualized Exp.*, 2018, **140**, 58151.
17 C. E. Byrne, K. M. Conrad, A. T. Martier, G. Fortes, G. W. Kpeli and E. Olsen, *et al.*, Adaptable Fabrication of Vascularized Milliscale Tissues in Membrane-Free Organ Chips Manufactured with 3D Printed Molds, *bioRxiv*, 2023, [cité 27 nov 2024], p. 2023.12.06.570409, Disponible sur: **https://www.biorxiv.org/content/10.1101/2023.12.06.570409v1**.
18 B. Venzac, S. Deng, Z. Mahmoud, A. Lenferink, A. Costa and F. Bray, *et al.*, PDMS Curing Inhibition on 3D-Printed Molds: Why? Also, How to Avoid It?, *Anal. Chem.*, 2021, **93**(19), 7180–7187.
19 M. de Almeida Monteiro Melo Ferraz, J. B. Nagashima, B. Venzac, S. Le Gac and N. Songsasen, 3D printed mold leachates in PDMS microfluidic devices, *Sci. Rep.*, 2020, **10**(1), 994.
20 H. J. Kim, D. Huh, G. Hamilton and D. E. Ingber, Human gut-on-a-chip inhabited by microbial flora that experiences intestinal peristalsis-like motions and flow, *Lab Chip*, 2012, **12**(12), 2165.
21 W. Shin, C. D. Hinojosa, D. E. Ingber and H. J. Kim, Human Intestinal Morphogenesis Controlled by Transepithelial Morphogen Gradient and Flow-Dependent Physical Cues in a Microengineered Gut-on-a-Chip, *iScience*, 2019, **15**, 391–406.
22 D. Ershov, M. S. Phan, J. W. Pylvänäinen, S. U. Rigaud, L. Le Blanc and A. Charles-Orszag, *et al.*, TrackMate 7: integrating

state-of-the-art segmentation algorithms into tracking pipelines, *Nat. Methods*, 2022, **19**(7), 829–832.

23 S. Salomé-Desnoulez, S. Poiret, B. Foligné, G. Muharram, V. Peucelle and F. Lafont, *et al.*, Persistence and dynamics of fluorescent Lactobacillus plantarum in the healthy versus inflamed gut, *Gut Microbes*, 2021, **13**(1), 1897374.

24 A. Grassart, V. Malardé, S. Gobaa, A. Sartori-Rupp, J. Kerns and K. Karalis, *et al.*, Bioengineered Human Organ-on-Chip Reveals Intestinal Microenvironment and Mechanical Forces Impacting Shigella Infection, *Cell Host Microbe*, 2019, **26**(3), 435–444.e4.

25 M. D. Abràmoff, P. J. Magalhães and S. J. Ram, Image processing with ImageJ, *Biophotonics Int.*, 2004, **11**(7), 36–42.

26 Y. C. Shin, W. Shin, D. Koh, A. Wu, Y. M. Ambrosini and S. Min, *et al.*, Three-Dimensional Regeneration of Patient-Derived Intestinal Organoid Epithelium in a Physiodynamic Mucosal Interface-on-a-Chip, *Micromachines*, 2020, **11**(7), 663.

27 P. Parthiban, S. Vijayan, P. S. Doyle and M. Hashimoto, Evaluation of 3D-printed molds for fabrication of non-planar microchannels, *Biomicrofluidics*, 2021, **15**(2), 024111.

28 A. Apostolou, R. A. Panchakshari, A. Banerjee, D. V. Manatakis, M. D. Paraskevopoulou and R. Luc, *et al.*, A Novel Microphysiological Colon Platform to Decipher Mechanisms Driving Human Intestinal Permeability, *Cell. Mol. Gastroenterol. Hepatol.*, 2021, **12**(5), 1719–1741.

29 C. Soragni, T. Vergroesen, N. Hettema, G. Rabussier, H. L. Lanz and S. J. Trietsch, *et al.*, Quantify permeability using on-a-chip models in high-throughput applications, *STAR Protoc.*, 2023, **4**(1), 102051.

30 H. J. Kim, H. Li, J. J. Collins and D. E. Ingber, Contributions of microbiome and mechanical deformation to intestinal bacterial overgrowth and inflammation in a human gut-on-a-chip, *Proc. Natl. Acad. Sci. U. S. A.*, 2016, **113**(1), E7–E15.

31 M. Arnoldini, J. Cremer and T. Hwa, Bacterial growth, flow, and mixing shape human gut microbiota density and composition, *Gut Microbes*, 2018, **9**(6), 559–566.

32 E. Secchi, A. Vitale, G. L. Miño, V. Kantsler, L. Eberl and R. Rusconi, *et al.*, The effect of flow on swimming bacteria controls the initial colonization of curved surfaces, *Nat. Commun.*, 2020, **11**(1), 2851.

33 J. Lee, N. V. Menon, H. D. Truong and C. T. Lim, Dynamics of Spatial Organization of Bacterial Communities in a Tunable Flow Gut Microbiome-on-a-Chip, *Small*, 2025, **21**(20), 2410258.

34 K. J. Krieger, N. Bertollo, M. Dangol, J. T. Sheridan, M. M. Lowery and E. D. O'Cearbhaill, Simple and customizable method for fabrication of high-aspect ratio microneedle molds using low-cost 3D printing, *Microsyst. Nanoeng.*, 2019, **5**(1), 1–14.

35 Y. Liu and H. Lu, Microfluidics in systems biology — hype or truly useful?, *Curr. Opin. Biotechnol.*, 2016, **39**, 215–220.

36 G. W. Kpeli, K. M. Conrad, W. Bralower, C. E. Byrne, S. M. Boue and M. E. Burow, *et al.*, Xenohormetic Phytochemicals Inhibit Neovascularization in Microphysiological Models of Vasculogenesis and Tumor Angiogenesis, *Adv. Biol.*, 2024, **8**(7), 2300480.

37 M. Ramasamy, B. Ho, C. M. Phan, N. Qin, C. L. Ren and L. Jones, Inexpensive and rapid fabrication of PDMS microfluidic devices for biological testing applications using low cost commercially available 3D printers, *J. Micromech. Microeng.*, 2023, **33**(10), 105016.

38 J. Zhang, W. Xu, F. Xu, W. Lu, L. Hu and J. Zhou, *et al.*, Microfluidic droplet formation in co-flow devices fabricated by micro 3D printing, *J. Food Eng.*, 2021, **290**, 110212.

39 M. Geiger, P. Marsico, D. Pensold, M. Wessling, G. Zimmer-Bensch and J. Linkhorst, A Microfluidic Perfusion Culture Setup to Investigate Cell Migration in 3D Constrictions, *Adv. Mater. Technol.*, 2024, **9**(6), 2301535.

40 M. W. Toepke and D. J. Beebe, PDMS absorption of small molecules and consequences in microfluidic applications, *Lab Chip*, 2006, **6**(12), 1484–1486.

41 H. Khoo, W. S. Allen, N. Arroyo-Currás and S. C. Hur, Rapid prototyping of thermoplastic microfluidic devices via SLA 3D printing, *Sci. Rep.*, 2024, **14**(1), 17646.

42 Light-based 3D printing and post-treatments of moulds for PDMS soft lithography - Lab on a Chip (RSC Publishing), [cité 5 juin 2025], Disponible sur: **https://pubs-rsc-org.insb.bib.cnrs.fr/en/content/articlelanding/2025/lc/d4lc00836g**.

43 M. Ramasamy, B. Ho, C. M. Phan, N. Qin, C. L. Ren and L. Jones, Inexpensive and rapid fabrication of PDMS microfluidic devices for biological testing applications using low cost commercially available 3D printers, *J. Micromech. Microeng.*, 2023, **33**(10), 105016.

44 A. Urrios, C. Parra-Cabrera, N. Bhattacharjee, A. M. Gonzalez-Suarez, L. G. Rigat-Brugarolas and U. Nallapatti, *et al.*, 3D-printing of transparent bio-microfluidic devices in PEG-DA, *Lab Chip*, 2016, **16**(12), 2287–2294.

45 N. Brandenberg and M. P. Lutolf, In Situ Patterning of Microfluidic Networks in 3D Cell-Laden Hydrogels, *Adv. Mater.*, 2016, **28**(34), 7450–7456.

46 M. Nikolaev, O. Mitrofanova, N. Broguiere, S. Geraldo, D. Dutta and Y. Tabata, *et al.*, Homeostatic mini-intestines through scaffold-guided organoid morphogenesis, *Nature*, 2020, **585**(7826), 574–578.

47 W. Shin and H. J. Kim, 3D in vitro morphogenesis of human intestinal epithelium in a gut-on-a-chip or a hybrid chip with a cell culture insert, *Nat. Protoc.*, 2022, **17**(3), 910–939.

48 O. Mitrofanova, M. Nikolaev, Q. Xu, N. Broguiere, I. Cubela and J. G. Camp, *et al.*, Bioengineered human colon organoids with in vivo-like cellular complexity and function, *Cell Stem Cell*, 2024, **31**(8), 1175–1186.e7.

49 S. L. Miles, K. E. Holt and S. Mostowy, Recent advances in modelling Shigella infection, *Trends Microbiol.*, 2024, **32**(9), 917–924.

50 A. Valiei, J. Aminian-Dehkordi and M. R. K. Mofrad, Gut-on-a-chip models for dissecting the gut microbiology and physiology, *APL Bioeng.*, 2023, **7**(1), 011502.

51 D. E. Ingber, Human organs-on-chips for disease modelling, drug development and personalized medicine, *Nat. Rev. Genet.*, 2022, **23**(8), 467–491.